Computational Mechanics manuscript No.
(will be inserted by the editor)

Wind turbine aerodynamics using ALE–VMS: Validation and the role of weakly enforced boundary conditions

Ming-Chen Hsu · Ido Akkerman · Yuri Bazilevs

Received: 18 October 2011 / Accepted: date

Abstract In this article we present a validation study involving the full-scale NREL Phase VI two-bladed wind turbine rotor. The ALE–VMS formulation of aerodynamics, based on the Navier–Stokes equations of incompressible flows, is employed in conjunction with weakly enforced essential boundary conditions. We find that the ALE–VMS formulation using linear tetrahedral finite elements is able to reproduce experimental data for the aerodynamic (low-speed shaft) torque and cross-section pressure distribution of the NREL Phase VI rotor. We also find that weak enforcement of essential boundary conditions is critical for obtaining accurate aerodynamics results on relatively coarse boundary layer meshes. The proposed numerical formulation is also successfully applied to the aerodynamics simulation of the NREL 5MW offshore baseline wind turbine rotor.

Keywords NREL Phase VI · NREL 5MW offshore · wind turbine aerodynamics · ALE–VMS · weakly enforced essential boundary conditions · finite elements

1 Introduction

Currently most wind turbine aerodynamics and aeroelasticity simulations are performed using low-fidelity methods, such as the Blade Element Momentum (BEM) theory for the rotor aerodynamics employed in conjunction with simplified structural models of the wind turbine blades and tower (see, e.g., [1, 2]). These methods are very fast to implement and execute, however, the cases involving unsteady flow, turbulence, 3D details of the wind turbine blade and tower geometry, etc., are beyond their range of applicability.

M.-C. Hsu · I. Akkerman · Y. Bazilevs (✉)
Department of Structural Engineering, University of California, San Diego, 9500 Gilman Drive, Mail Code 0085, La Jolla, CA 92093, USA
E-mail: yuri@ucsd.edu

In recent years, several attempts were made to address the above mentioned challenges and to raise the fidelity and predictability levels of wind turbine simulations. Standalone aerodynamics simulations of wind turbine configurations in 3D were reported in [3–11], while standalone structural analyses of rotor blades of complex geometry and material composition, but under assumed wind load conditions or wind load conditions coming from separate aerodynamic computations were reported in [12–17]. In the recent work of [18] it was shown that coupled fluid–structure interaction (FSI) modeling and simulation of wind turbines is important in order to accurately predict their mechanical behavior at full scale.

We simulated the NREL 5MW offshore baseline wind turbine rotor in [9, 10, 18–20], and compared the results with those reported in [2]. Although good matching of the aerodynamic torque was obtained in the case of steady inflow and rotor speed conditions, this was not, strictly speaking, validation, since the comparison was made with another numerical simulation. In this work, we perform a true validation study in which we compare our aerodynamics simulation results with the results of the experiments performed on a two-bladed NREL Phase VI rotor [21]. The rotor geometry definition and experimental data for the aerodynamic (low-speed shaft) torque and blade cross-section pressure distribution were reported in [21–23] for a variety of test conditions. Here we perform a comparison for a subset of these tests.

This paper is outlined as follows. In Section 2, we introduce the Arbitrary Lagrangian–Eulerian (ALE) form of the Navier–Stokes equations of incompressible flow suitable for moving domain problems. We also present the residual-based variational multiscale (VMS) formulation of the Navier–Stokes equations and turbulence modeling [24], which we refer to as the ALE–VMS method. In this work, the ALE–VMS equations are discretized using linear tetra-

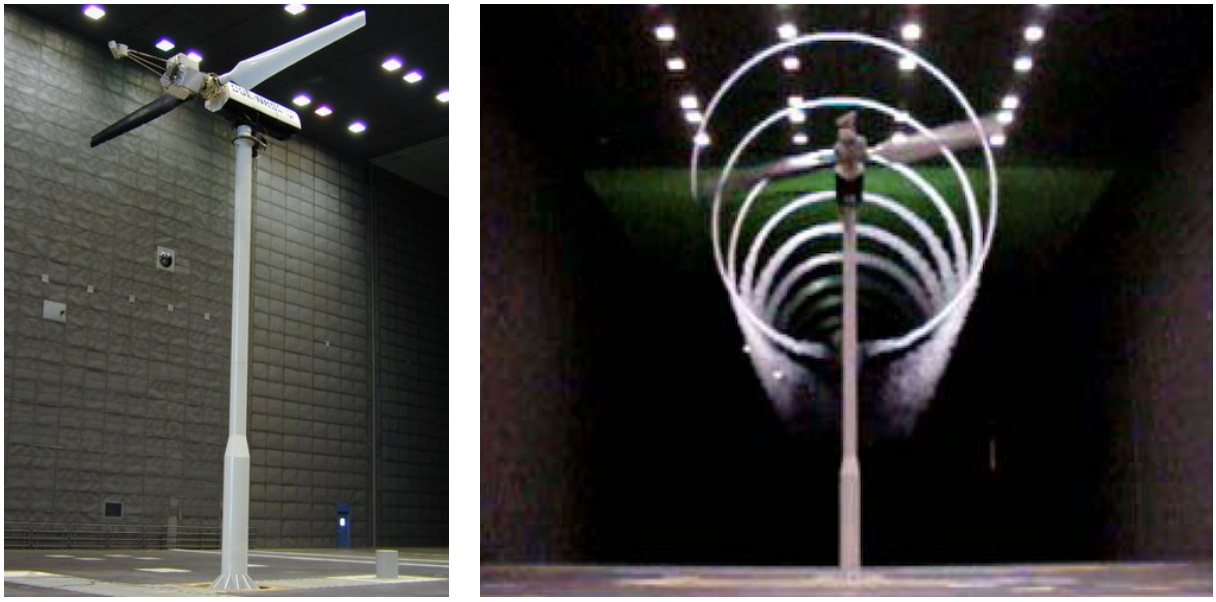

(a) (b)

Fig. 1 (a) NREL UAE Phase VI wind turbine mounted in NASA Ames 80 ft × 120 ft wind tunnel. (b) Wake flow visualization of the operating turbine in the wind tunnel. The images are taken from [21].

hedral finite elements in space. This is in contrast to our earlier work on wind turbine simulation, where Isogeometric Analysis [25, 26] was used for both aerodynamics and FSI computations. The ALE–VMS formulation is augmented with weakly enforced essential boundary conditions, which were first proposed in [27] and further improved and studied in [28–30]. The weak boundary condition formulation may thought of as an extension of Nitsche's method [31] to the case of the Navier–Stokes equations of incompressible flow. Another interpretation of the weak boundary condition formulation is that it is a Discontinuous Galerkin method (see, e.g., [32]), where the continuity of the basis functions is enforced everywhere in the domain interior, but not at the domain boundary. In Section 3, we present the simulation results. We first perform the simulations for the NREL Phase VI two-bladed rotor. Both weakly and strongly enforced no-slip and no-penetration boundary conditions are employed in these simulations. For the cases considered, very good matching with the experimental results is obtained for the aerodynamic torque and pressure distribution on the blade axial cross-sections when weakly enforced boundary condition formulation is employed. We then simulate the NREL 5MW offshore baseline wind turbine rotor and obtain very good agreement with the NURBS-based isogeometric analysis computations of this test case from [9, 18], as well as predictions from [2]. In Section 4, we draw conclusions and outline future developments.

2 ALE–VMS formulation of the Navier–Stokes equations of incompressible flow

2.1 Continuous problem

Let $\Omega_t \in \mathbb{R}^d$, $d = 2, 3$, be the spatial domain of the aerodynamics problem with boundary Γ_t at time $t \in (0, T)$. The subscript t indicates that the fluid mechanics spatial domain is time-dependent. The Navier–Stokes equations of incompressible flow in the Arbitrary Lagrangian-Eulerian (ALE) frame may be written on Ω_t and $\forall t \in (0, T)$ as

$$\rho\left(\left.\frac{\partial \mathbf{u}}{\partial t}\right|_{\hat{x}} + (\mathbf{u} - \hat{\mathbf{u}}) \cdot \boldsymbol{\nabla}_x \mathbf{u} - \mathbf{f}\right) - \boldsymbol{\nabla}_x \cdot \boldsymbol{\sigma} = \mathbf{0},$$
$$\boldsymbol{\nabla}_x \cdot \mathbf{u} = 0, \tag{1}$$

where ρ, $\mathbf{u}$, and $\mathbf{f}$ are the density, velocity and the external force (per unit mass), respectively, and the stress tensor $\boldsymbol{\sigma}$ is defined as

$$\boldsymbol{\sigma}(\mathbf{u}, p) = -p\mathbf{I} + 2\mu\boldsymbol{\varepsilon}(\mathbf{u}). \tag{2}$$

Here p is the pressure, $\mathbf{I}$ is the identity tensor, μ is the dynamic viscosity, and $\boldsymbol{\varepsilon}(\mathbf{u})$ is the strain-rate tensor given by

$$\boldsymbol{\varepsilon}(\mathbf{u}) = \frac{1}{2}\left(\boldsymbol{\nabla}_x \mathbf{u} + \boldsymbol{\nabla}_x \mathbf{u}^T\right). \tag{3}$$

In Eq. (1), $\left|_{\hat{x}}\right.$ denotes the fact that the time derivative is taken with respect to a fixed referential domain spatial coordinates $\hat{\mathbf{x}}$, and $\hat{\mathbf{u}}$ is the velocity of the fluid domain Ω_t. The spatial gradients are taken with respect to the spatial coordinates $\mathbf{x}$ of the current configuration, which is reflected in the subscript on the gradient operator.

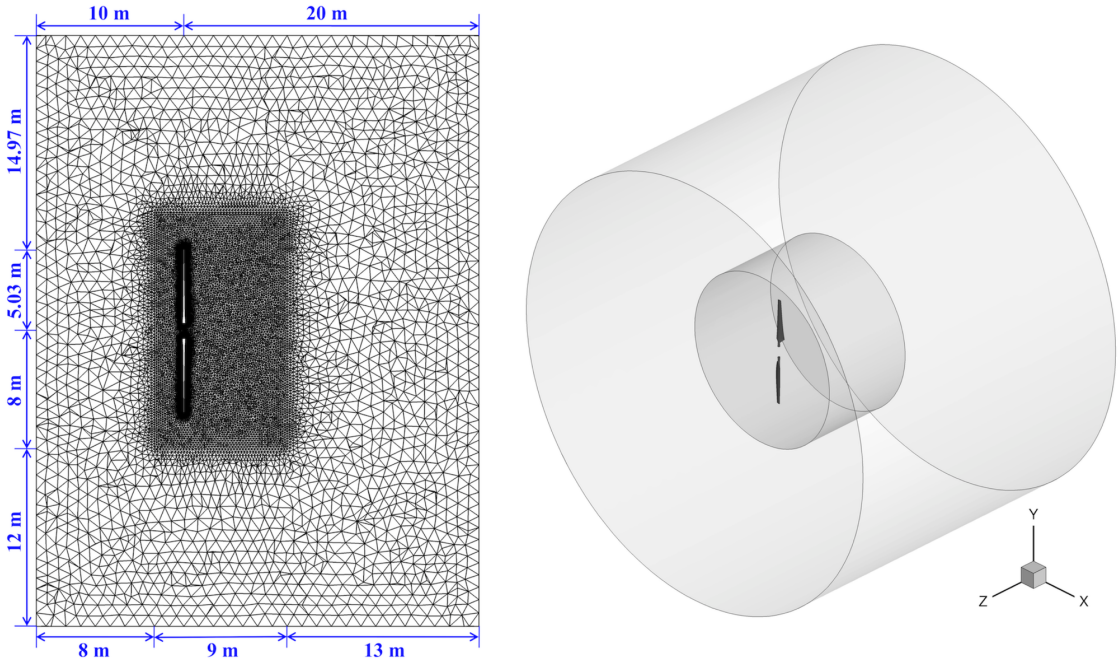

Fig. 2 NREL Phase VI wind turbine. The problem mesh and computational domain. The ratio of the rotor radius to the radius and the axial length of the computational domain are approximately 1/4 and 1/6, respectively. The mesh is refined in the inner region for better flow resolution near the rotor.

2.2 ALE–VMS formulation

The ALE–VMS formulation of the continuum aerodynamics formulation is given by: find $\mathbf{u}^h \in \mathcal{S}_u^h$ and $p^h \in \mathcal{S}_p^h$, such that $\forall \mathbf{w}^h \in \mathcal{V}_u^h$ and $\forall q^h \in \mathcal{V}_p^h$

$$
\begin{aligned}
&\int_{\Omega_t} \mathbf{w}^h \cdot \rho \left(\left. \frac{\partial \mathbf{u}^h}{\partial t} \right|_{\hat{x}} + \left(\mathbf{u}^h - \hat{\mathbf{u}}^h\right) \cdot \boldsymbol{\nabla}_x \mathbf{u}^h - \mathbf{f} \right) \mathrm{d}\Omega \\
&+ \int_{\Omega_t} \boldsymbol{\varepsilon}\left(\mathbf{w}^h\right) \,:\, \boldsymbol{\sigma}\left(\mathbf{u}^h, p^h\right) \mathrm{d}\Omega \\
&- \int_{(\Gamma_\mathrm{h})_t} \mathbf{w}^h \cdot \mathbf{h} \, \mathrm{d}\Gamma + \int_{\Omega_t} q^h \boldsymbol{\nabla}_x \cdot \mathbf{u}^h \, \mathrm{d}\Omega \\
&+ \sum_{e=1}^{N_\mathrm{el}} \int_{\Omega_t^e} \tau_\mathrm{SUPS} \left(\left(\mathbf{u}^h - \hat{\mathbf{u}}^h\right) \cdot \boldsymbol{\nabla}_x \mathbf{w}^h + \frac{\boldsymbol{\nabla}_x q^h}{\rho} \right) \cdot \mathbf{r}_\mathrm{M}\left(\mathbf{u}^h, p^h\right) \mathrm{d}\Omega \\
&+ \sum_{e=1}^{N_\mathrm{el}} \int_{\Omega_t^e} \rho \nu_\mathrm{LSIC} \boldsymbol{\nabla}_x \cdot \mathbf{w}^h r_\mathrm{C}(\mathbf{u}^h, p^h) \, \mathrm{d}\Omega \\
&- \sum_{e=1}^{N_\mathrm{el}} \int_{\Omega_t^e} \tau_\mathrm{SUPS} \mathbf{w}^h \cdot \left(\mathbf{r}_\mathrm{M}\left(\mathbf{u}^h, p^h\right) \cdot \boldsymbol{\nabla}_x \mathbf{u}^h \right) \mathrm{d}\Omega \\
&- \sum_{e=1}^{N_\mathrm{el}} \int_{\Omega_t^e} \frac{\boldsymbol{\nabla}_x \mathbf{w}^h}{\rho} \,:\, \left(\tau_\mathrm{SUPS} \mathbf{r}_\mathrm{M}\left(\mathbf{u}^h, p^h\right)\right) \otimes \left(\tau_\mathrm{SUPS} \mathbf{r}_\mathrm{M}\left(\mathbf{u}^h, p^h\right)\right) \mathrm{d}\Omega \\
&= 0.
\end{aligned}
\tag{4}
$$

Here, the time-dependent fluid domain Ω_t is divided into N_el individual spatial finite element subdomains denoted by Ω_t^e. The finite element spaces $\mathcal{S}_u^h$ for the velocity and $\mathcal{S}_p^h$ for the pressure, as well as the corresponding test function spaces $\mathcal{V}_u^h$ and $\mathcal{V}_p^h$ are assumed to be of equal order, and, in this work, are comprised of piece-wise linear polynomials, which are continuous at the inter-element boundaries of the tetrahedral mesh. In Eq. (4), $\mathbf{h}$ is the natural boundary condition, $(\Gamma_\mathrm{h})_t$ is the part of the boundary where we specify that natural boundary condition, $\hat{\mathbf{u}}^h$ is the mesh velocity, and $\mathbf{r}_\mathrm{M}$ and r_C are the residuals of the momentum and continuity (incompressibility constraint) equations, respectively, given by

$$
\begin{aligned}
\mathbf{r}_\mathrm{M}(\mathbf{u}^h, p^h) = \rho \left(\left. \frac{\partial \mathbf{u}^h}{\partial t} \right|_{\hat{x}} + \left(\mathbf{u}^h - \hat{\mathbf{u}}^h\right) \cdot \boldsymbol{\nabla}_x \mathbf{u}^h - \mathbf{f}^h \right) \\
- \boldsymbol{\nabla}_x \cdot \boldsymbol{\sigma}\left(\mathbf{u}^h, p^h\right)
\end{aligned}
\tag{5}
$$

and

$$
r_\mathrm{C}(\mathbf{u}^h, p^h) = \boldsymbol{\nabla}_x \cdot \mathbf{u}^h. \tag{6}
$$

Also in Eq. (4), τ_SUPS and ν_LSIC are the stabilization parameters defined in [33] as

$$
\tau_\mathrm{SUPS} = \left(\frac{4}{\Delta t^2} + \left(\mathbf{u}^h - \hat{\mathbf{u}}^h\right) \cdot \mathbf{G} \left(\mathbf{u}^h - \hat{\mathbf{u}}^h\right) + C_I \nu^2 \mathbf{G} : \mathbf{G} \right)^{-1/2} \tag{7}
$$

and

$$
\nu_\mathrm{LSIC} = \left(\mathrm{tr}\mathbf{G} \, \tau_\mathrm{SUPS}\right)^{-1}, \tag{8}
$$

where

$$
\mathrm{tr}\mathbf{G} = \sum_{i=1}^{d} G_{ii} \tag{9}
$$

is the trace of the element metric tensor $\mathbf{G}$, Δt is the time-step size, and C_I is a positive constant, independent of the mesh size, derived from an appropriate element-wise inverse estimate (see, e.g., [34–36]).

Remark 1 *The stabilization parameters τ_{SUPS} and ν_{LSIC} in the above equations originate from stabilized finite element methods for fluid dynamics (see, e.g., [37–43]). The notation "SUPS", introduced in [44], indicates that there is a single stabilization parameter for the SUPG and PSPG stabilizations, instead of two separate parameters. The notation "LSIC", introduced in [41], denotes the stabilization based on least-squares on the incompressibility constraint. The stabilization parameters were designed and studied extensively in the context of stabilized finite element formulations of linear model problems of direct relevance to fluid mechanics. These model problems include advection–diffusion and Stokes equations. The design of τ_{SUPS} and ν_{LSIC} is such that optimal convergence with respect to the mesh size and polynomial order of discretization is attained for these cases (see, e.g., [43] and references therein). Furthermore, enhanced stability for advection-dominated flows and the ability to conveniently employ the same basis functions for velocity and pressure variables for incompressible flow are some of the attractive outcomes of this method. More recently, the stabilization parameters were derived in the context of the variational multiscale methods [45, 46] and were interpreted as the appropriate averages of the small-scale Green's function, a key mathematical object in the theory of VMS methods (see [47] for an elaboration). The ALE–VMS formulation is a moving-domain extension of the residual-based variational multiscale (RBVMS) turbulence modeling technique proposed for stationary domains in [24]. It was also presented in [33] for moving domains in the context of FSI. Recently, in [44], the authors extended the RBVMS formulation for moving domain problems using the space–time finite element method.*

2.3 Weakly enforced essential boundary conditions

In this section we state the formulation of the weakly enforced essential boundary conditions. These were first proposed for the advection–diffusion equation and for the Navier–Stokes equations of incompressible flow in [27] in an effort to improve the accuracy of stabilized and multiscale formulations in the presence of thin unresolved boundary layers. The idea of weak enforcement of essential boundary conditions emanates from the work of Nitsche [31] and the developments in discontinuous Galerkin methods. In [28–30], the weak boundary condition formulation was further refined and studied on a set of important and challenging wall-bounded turbulent flows. In this work, we apply weakly enforced essential boundary condition formulation to the problem of aerodynamics of wind turbines at full spatial scale.

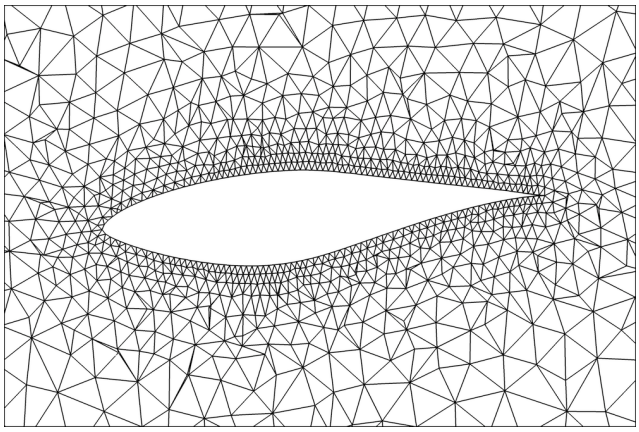

Fig. 3 NREL Phase VI wind turbine. A 2D blade cross-section at $0.8R$ to illustrate the type of mesh near the boundary that we used in our computation. The size of the first element in the wall-normal direction is about 0.008 m.

To account for the weak enforcement of essential boundary conditions, we remove them from the trial and test function sets $\mathcal{S}_u^h$ and $\mathcal{V}_u^h$, and add the following terms to the left-hand-side of Eq. (4)

$$
\begin{aligned}
&-\sum_{b=1}^{N_{\text{eb}}}\int_{\Gamma^b\cap(\Gamma_{\text{g}})_t}\mathbf{w}^h\cdot\boldsymbol{\sigma}\left(\mathbf{u}^h,p^h\right)\mathbf{n}\,\mathrm{d}\Gamma\\
&-\sum_{b=1}^{N_{\text{eb}}}\int_{\Gamma^b\cap(\Gamma_{\text{g}})_t}\left(2\mu\boldsymbol{\varepsilon}\left(\mathbf{w}^h\right)\mathbf{n}+q^h\mathbf{n}\right)\cdot\left(\mathbf{u}^h-\mathbf{g}\right)\,\mathrm{d}\Gamma\\
&-\sum_{b=1}^{N_{\text{eb}}}\int_{\Gamma^b\cap(\Gamma_{\text{g}})_t^-}\mathbf{w}^h\cdot\rho\left(\left(\mathbf{u}^h-\hat{\mathbf{u}}^h\right)\cdot\mathbf{n}\right)\left(\mathbf{u}^h-\mathbf{g}\right)\,\mathrm{d}\Gamma\\
&+\sum_{b=1}^{N_{\text{eb}}}\int_{\Gamma^b\cap(\Gamma_{\text{g}})_t}\tau_{\text{TAN}}^B\left(\mathbf{w}^h-\left(\mathbf{w}^h\cdot\mathbf{n}\right)\mathbf{n}\right)\\
&\qquad\qquad\cdot\left(\left(\mathbf{u}^h-\mathbf{g}\right)-\left(\left(\mathbf{u}^h-\mathbf{g}\right)\cdot\mathbf{n}\right)\mathbf{n}\right)\,\mathrm{d}\Gamma\\
&+\sum_{b=1}^{N_{\text{eb}}}\int_{\Gamma^b\cap(\Gamma_{\text{g}})_t}\tau_{\text{NOR}}^B\left(\mathbf{w}^h\cdot\mathbf{n}\right)\left(\left(\mathbf{u}^h-\mathbf{g}\right)\cdot\mathbf{n}\right)\,\mathrm{d}\Gamma.
\end{aligned}
\tag{10}
$$

Here $\left(\Gamma_{\text{g}}\right)_t$ is a part of the fluid domain boundary where we set the velocity boundary conditions given by $\mathbf{g}$. $\left(\Gamma_{\text{g}}\right)_t$ is decomposed into N_{eb} surface elements, and $\left(\Gamma_{\text{g}}\right)_t^-$ is defined as the "inflow" part of $\left(\Gamma_{\text{g}}\right)_t$ as

$$
\left(\Gamma_{\text{g}}\right)_t^- = \left\{\mathbf{x}\;\middle|\;\left(\mathbf{u}^h-\hat{\mathbf{u}}^h\right)\cdot\mathbf{n}<0,\;\forall\mathbf{x}\subset\left(\Gamma_{\text{g}}\right)_t\right\}. \tag{11}
$$

If $\left(\Gamma_{\text{g}}\right)_t$ coincides with the moving wall (rigid or flexible), then $\mathbf{g}$ is the prescribed wall velocity.

The structure of the terms in Eq. (10) is as follows. The term on the first line is the so-called consistency term. It

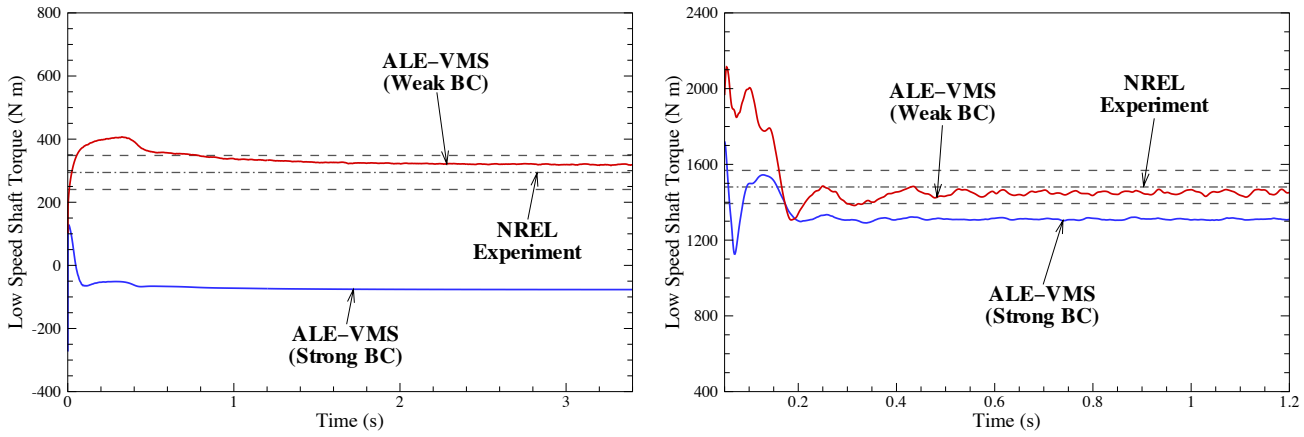

(a) 5 m/s case (b) 25 m/s case

Fig. 4 NREL Phase VI wind turbine. The time history of the aerodynamic (low-speed shaft) torque for both weak and strong boundary condition simulations for (a) 5 m/s and (b) 25 m/s cases. The results are compared to the NREL experimental data reported in [3,48]. Dashed line represents the experimental standard deviation to indicated the variation over one revolution

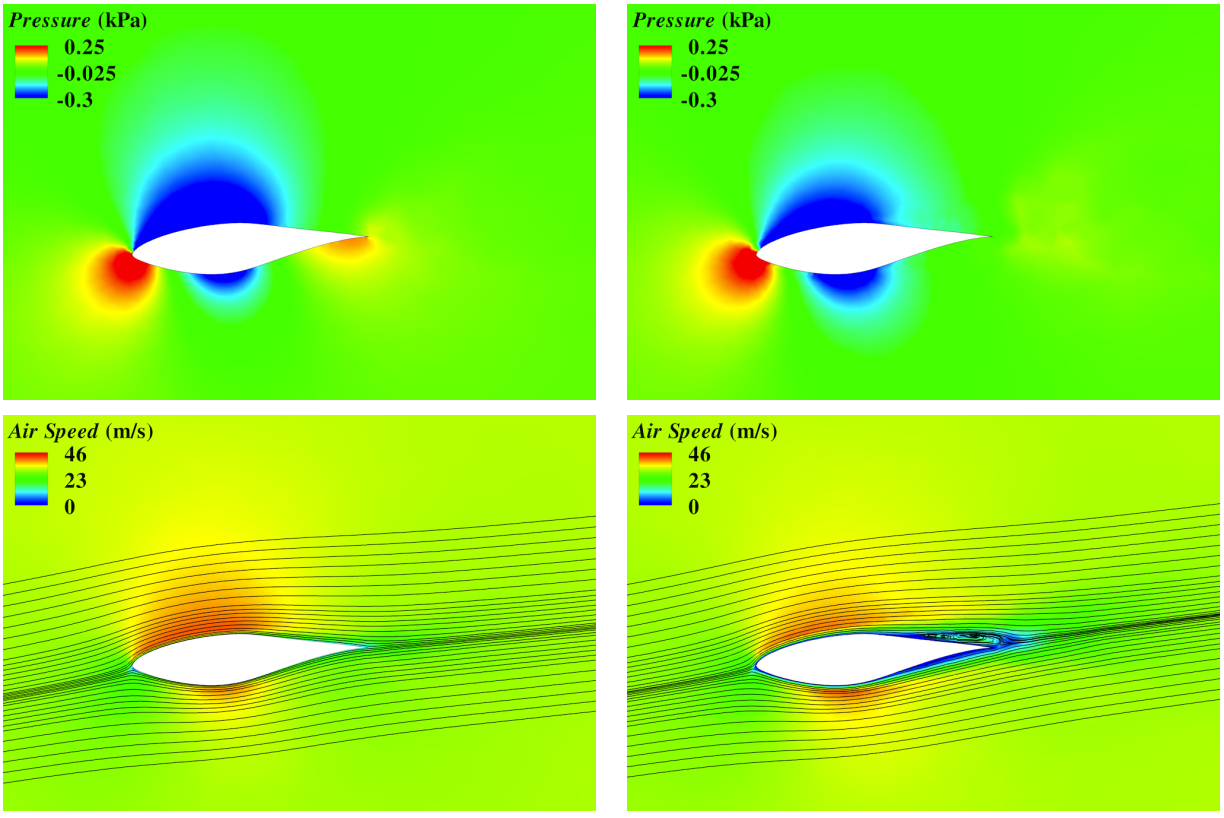

(a) Weakly enforced boundary condition (b) Strongly enforced boundary condition

Fig. 5 NREL Phase VI wind turbine. Pressure and air speed contours and velocity streamlines at $0.8R$ for 5 m/s case: (a) Weakly enforced boundary condition simulation. (b) Strongly enforced boundary condition simulation.

is necessary to ensure that the discrete formulation is identically satisfied by the exact solution of the Navier–Stokes equations, which, in turn, has implications on the accuracy of the discrete formulation. Also note that this term cancels with the terms which come from the integration-by-parts of the stress terms in Eq. (4), thus correctly removing traction boundary conditions from the no-slip boundary. The term on the second line is the so-called adjoint consistency term. It's role is less intuitive, as it ensures that the analytical solution of the adjoint equations, when introduced in place of

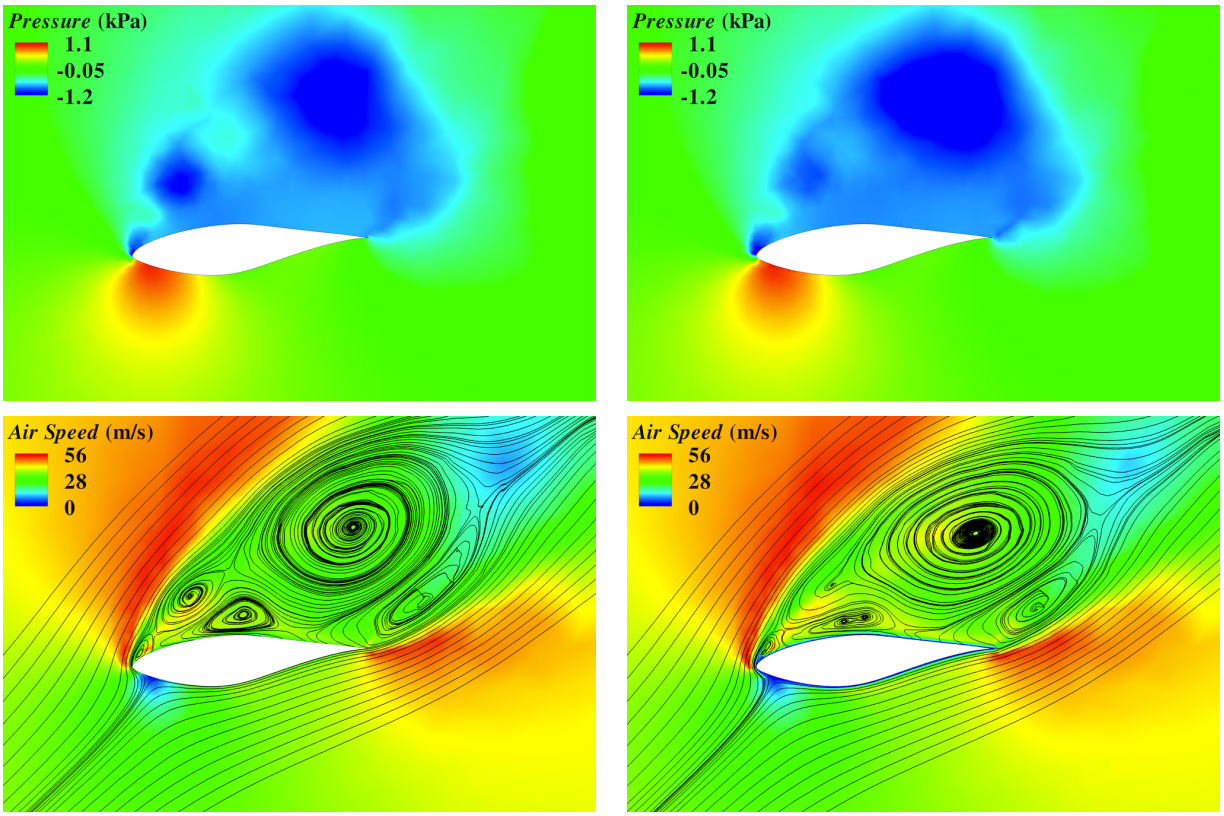

(a) Weakly enforced boundary condition (b) Strongly enforced boundary condition

Fig. 6 NREL Phase VI wind turbine. Pressure and air speed contours and velocity streamlines at $0.8R$ for 25 m/s case: (a) Weakly enforced boundary condition simulation. (b) Strongly enforced boundary condition simulation.

the linear momentum and continuity equation test functions, also satisfies the discrete formulation. Adjoint consistency is linked to optimal convergence of the discrete solution in lower-order norms (see, e.g., [32]). The term on the third line leads to better satisfaction of inflow boundary conditions. The last two terms are penalty-like, in that they penalize the deviation of the discrete solution from its prescribed value at the boundary. These terms are necessary to ensure the stability (or coercivity) of the discrete formulation, which may be lost due to the introduction of consistency and adjoint consistency terms.

The weak boundary condition formulation is numerically stable if

$$\tau^B_{\text{TAN}} = \tau^B_{\text{NOR}} = \frac{C^B_I \mu}{h_n}, \tag{12}$$

where h_n is the wall-normal element size, and C^B_I is a sufficiently large positive constant, which is computed from an appropriate element-level inverse estimate (see, e.g., [34–36]). C^B_I depends on the space dimension d, the element type (tetrahedron, hexahedron, etc.), and the polynomial order of the finite element approximation. For a linear tetrahedron, it is sufficient to take $4.0 \leq C^B_I \leq 8.0$ to obtain a stable discrete solution. The wall-normal element size may be computed from the element metric tensor as

$$h_n = (\mathbf{n} \cdot \mathbf{G}\mathbf{n})^{-1/2}, \tag{13}$$

where $\mathbf{n}$ is the outward wall-normal unit vector.

Remark 2 *Rather than setting the no-slip boundary conditions exactly, the weak boundary condition formulation gives the no-slip solution only in the limit as $h_n \to 0$. As a result, coarse boundary layer discretizations do not need to struggle to resolve thin boundary layers; the flow simply slips on the solid boundary. Because of this added flexibility, the weak boundary condition enforcement approach tends to produce more accurate results on meshes that are too coarse to capture the boundary layer solution. However, as the mesh is refined to capture the boundary layer, both weak and strong boundary condition formulations produce nearly identical results (see [28]).*

Remark 3 *Although the weak boundary condition formulation is also stable for very large values of C^B_I, we do not advocate this choice. Large values of C^B_I place a heavy penalization on the no-slip condition, and the above mentioned flexibility of the method is lost together with the associated accuracy benefits. We advocate using C^B_I that is just large*

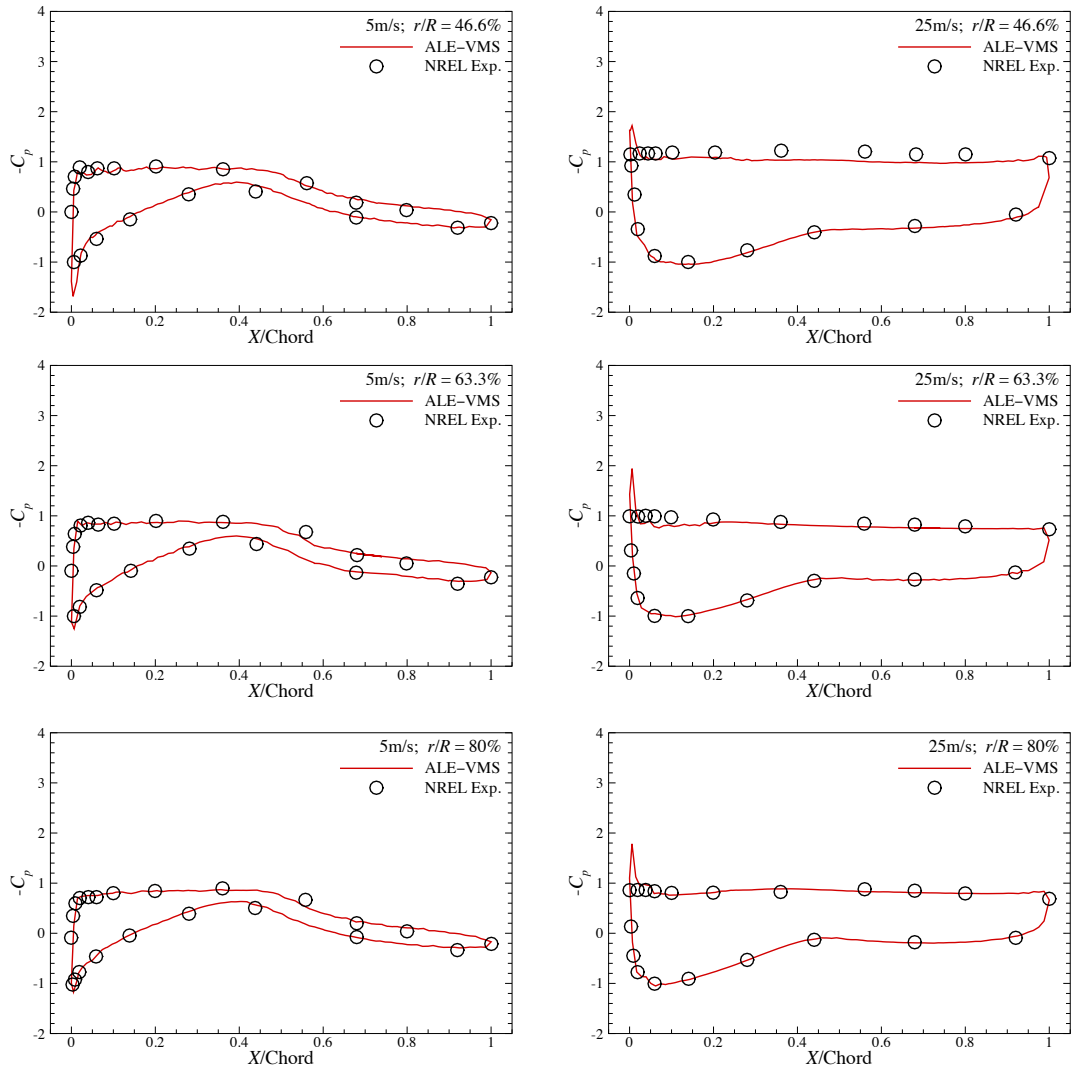

(a) 5 m/s case (b) 25 m/s case

Fig. 7 NREL Phase VI wind turbine. Pressure coefficients at $0.466R$, $0.633R$ and $0.8R$ for (a) 5 m/s and (b) 25 m/s cases. The predicted values (using the weak boundary condition formulation) are plotted against the experimental data reported in [3,48].

enough to guarantee the stability of the discrete formulation.

Remark 4 *In references [28], a connection was identified between weakly enforced boundary conditions and wall functions. The latter are commonly employed in conjunction with RANS formulations of turbulent flow (see, e.g., [49, 50]). In the case of wall function formulation, the no-slip boundary condition is replaced with a tangential traction boundary condition, where the traction direction is given by that of the local slip velocity, and the traction magnitude is computed by invoking the "law-of-the-wall", which is an empirical relationship between the flow speed and the normal distance to the wall, both appropriately normalized (see, e.g., [49]). The penalty parameter τ^B_{TAN} may be defined as*

$$\tau^B_{TAN} = \frac{\rho u^{*2}}{\|\mathbf{u}^h_{TAN}\|}, \tag{14}$$

where $\mathbf{u}^h_{TAN} = \big(\big(\mathbf{u}^h - \mathbf{g}\big) - \big(\big(\mathbf{u}^h - \mathbf{g}\big)\cdot\mathbf{n}\big)\mathbf{n}\big)$ is the tangential slip velocity, and u^* is the so-called friction velocity, which, among other factors, depends on the magnitude of the slip velocity, and is computed from the law-of-the-wall formula by means of a nonlinear iteration. It was shown in [28], however, that when the boundary layer mesh is fine enough, τ^B_{TAN} from Eq. (14) is independent of the local flow solution, and reverts to the definition given by Eq. (12). This fact is remarkable in that Eq. (12) is purely based on considerations of numerical stability, while Eq. (14) derives from physics of wall-bounded turbulent flows. In our limited experience,

both the "numerics-based" and "physics-based" definitions of the penalty parameter τ_{TAN}^{B} give very similar results.

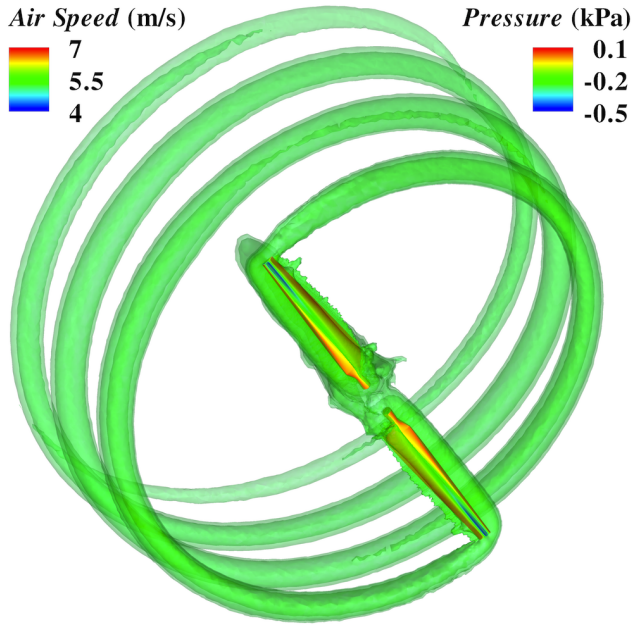

Fig. 8 NREL Phase VI wind turbine. Isosurfaces of air speed at an instant for 5 m/s case. The tip vortex generated by the blade is carried downstream of the rotor with little decay. Pressure contours are also plotted on the rotor surface.

3 Computational results

3.1 NREL Unsteady Aerodynamics Experiment Phase VI

The proposed ALE–VMS method is applied to predict the aerodynamics of the Unsteady Aerodynamics Experiment (UAE) Phase VI two-bladed wind turbine rotor [21] from the National Renewable Energy Laboratory (NREL). In this experiment, a two-bladed twisted and tapered 10.058 m diameter wind turbine, which has a rated power of 19.8 kW, was tested in the NASA Ames 80 ft × 120 ft wind tunnel in 2000 (see Figure 1). This is one of the most comprehensive, accurate and reliable experiments carried out on a full-scale wind turbine. This test case was also studied by many computational researchers [3–6,8,11,48,51–58] for the purposes of validating their simulation software and improving their ability to predict wind turbine aerodynamic performance.

The Phase VI rotor geometry makes use of a single NREL S809 airfoil [21]. Selected blade cross-section geometry data are summarized in Table 1. The detailed documentation of the rotor configuration and its technical specifications are available in [21]. Two cases from the experiment were selected for the validation study. The first case has wind speed of 5 m/s and the second case has wind speed of 25 m/s. For both cases, we have upwind configuration, 0° yaw angle, 0° cone angle, blade tip pitch angle of 3°, and rotational speed of 72 rpm. The influence of the hub and tower on the rotor aerodynamics was neglected, which is a fair approximation for an upwind turbine (see, e.g., [3]). The two cases we considered here present very different flow conditions. For the 5 m/s case the flow is fully attached for the entire blade. On the contrary, stall occurred for most of the blade for the case of 25 m/s wind, and reference [11] considered this case to be more challenging for simulation.

The wind turbine rotor radius R is 5.029 m and the blade is assumed to be rigid. The aerodynamic computation with prescribed wind and rotor speeds is carried out on a rotating mesh. The mesh resolution and computational domain are shown in Figure 2. The ratio of the rotor radius to the radius and the axial length of the computational domain are approximately 1/4 and 1/6, respectively. The mesh is refined in the inner region for better flow resolution near the rotor. At the inflow boundary the wind speed is set to either 5 m/s or 25 m/s. At the outflow boundary the traction vector is set to zero. At the radial boundary the radial component of the velocity is set to zero. The air density and viscosity are 1.23 kg/m^3 and 1.78×10^{-5} kg/(m·s), respectively. The Reynolds number based on the chord length and relative speed at $0.8R$ is $O(10^6)$.

The mesh is comprised of 8,494,182 linear tetrahedral elements and 1,508,983 nodes. Figure 3 shows a 2D blade cross-section at $0.8R$ to illustrate the type of mesh near the boundary that we used in our computation. Near the blade surface at $0.8R$, the size of the first element in the wall-normal direction is about 0.008 m, and the corresponding y^+ is $O(10^3)$. No special boundary layer meshing was used in this study, in part to test the ability of the ALE–VMS method to deal with coarse boundary layer meshes.

The computations were carried out in a parallel computing environment on a Dell Cluster at the Texas Advanced Computing Center (TACC) [59]. The system consists of 256 dual-socket nodes, each with 2 Intel Nehalem quad-core processors (8 cores) @ 2.53 GHz. Total system resources include 2048 compute cores, 14.5 TB aggregate memory, 512 GPUs, QDR InfiniBand interconnect, and an attached Lustre Parallel file system [60]. The mesh is partitioned into 128 subdomains using METIS [61] and each subdomain is assigned to a compute core. The parallel implementation of the methodology can be found in [19].

The ALE–VMS formulation is advanced in time using the Generalized-α method (see [33,62,63]). The linear system is solved using a block-diagonal preconditioned GMRES method [64,65]. The time-step size is 0.0001 s. The number of Newton's iterations per time step is 3 with 50 GMRES iterations for the first and second nonlinear iterations, and 50 to 80 GMRES iterations for the third nonlinear iteration depending on the nonlinear convergence. In

Radial Distance r (m)	Span Station (r/5.029 m)	Chord Length (m)	Twist (degrees)	Twist Axis (% chord)	Airfoil (-)
0.508	0.100	0.218	0.0	50	Cylinder
1.510	0.300	0.711	14.292	30	NREL S809
2.343	0.466	0.627	4.715	30	NREL S809
3.185	0.633	0.542	1.115	30	NREL S809
4.023	0.800	0.457	-0.381	30	NREL S809
4.780	0.950	0.381	-1.469	30	NREL S809
5.029	1.000	0.355	-1.815	30	NREL S809

Table 1 Selected blade cross-section geometry data for NREL UAE Phase VI rotor. For the complete table, please see [21,51]. Note that in [21], the information for the standard tip (r = 5.029) is not documented. However, it can be found in [51]

general, it takes about 20 to 24 hours to compute 1 s of real time, which is generally sufficient to predict the aerodynamic torque.

The time history of aerodynamic (low-speed shaft) torque is shown in Figure 4. Good agreement of the aerodynamic torque is found between the weak boundary condition simulations and experimental data for both flow conditions. However, the results for the strongly enforced boundary condition simulations are not at all accurate.

Pressure and air speed contours and velocity streamlines at 0.8R for 5 m/s and 25 m/s cases are shown in Figures 5 and 6, respectively. Figure 5a shows the weak boundary condition prediction of the air flow for the 5 m/s case. Here, the flow is fully attached, and the torque is correctly predicted. However, the strong boundary condition simulation predicts flow separation at the trailing edge (see Figure 5b). The blade stalls and, as a result, the torque is underpredicted by 126% (see Figure 4a). For the 25 m/s case, small differences are found in the pressure contours and air flow patterns between the weak and strong boundary condition computations. This is due to the fact that the flow is already separated at the edges, the entire airfoil is stalled, and the boundary layer resolution is not so important for these type of flow conditions. In this case, the weak boundary condition again correctly predicts the torque, while the strong boundary condition underpredicts the torque, but only by 11% (see Figure 4b).

These results are not surprising. In the case of strongly enforced boundary conditions, the coarse boundary layer discretization gives rise to artificially "thick" boundary layers, which retard the flow and lead to non-physical aerodynamics, such as premature flow separation. In the case of weakly enforced boundary conditions, the flow is allowed to slip on the solid surface without forming these undesired thick boundary layers. Of course, with sufficient boundary layer mesh refinement, both approaches will capture the boundary layer, and the strongly enforced boundary condition approach will also produce the correct result (see [28]).

Figure 7 shows the pressure coefficient at 0.466R, 0.633R and 0.8R for 5 m/s and 25 m/s cases. The predicted values (using the weak boundary condition formulation) are plotted against the experimental data. Very good agreement is likewise achieved for both attached and separated flow conditions at different radial locations.

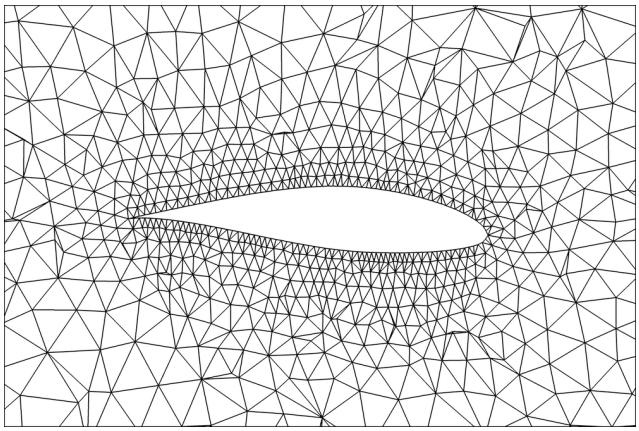

Fig. 9 NREL 5MW offshore baseline wind turbine. A 2D blade cross-section cut at 0.75R to illustrate the coarse boundary layer mesh used in our computations. Near the blade surface, the size of the first element in the wall-normal direction is about 0.075 m.

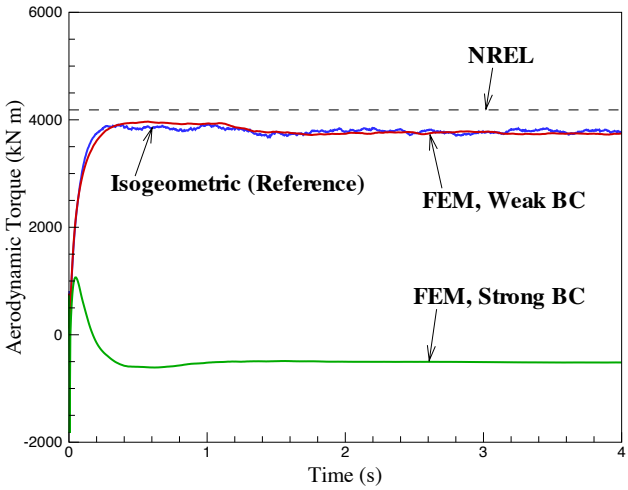

Fig. 10 NREL 5MW offshore baseline wind turbine. The time history of the aerodynamic torque for both weak and strong boundary condition simulations. The results are compared to the NURBS-based simulation from [19] and the NREL prediction from [2] obtained using FAST [1].

Figure 8 shows the flow visualization (isosurfaces of air speed) of the 5 m/s case. The tip vortex generated by the

blade is carried downstream of the rotor with little decay. Pressure contours are also plotted on the rotor surface in the figure.

3.2 NREL 5MW offshore baseline wind turbine

In this section, we present our computations of the NREL 5MW offshore baseline wind turbine rotor [2,9]. The NREL 5MW offshore baseline wind turbine is a conventional three-bladed upwind turbine proposed in [2] to support concept studies aimed at assessing offshore wind technology. The detailed geometry description and construction for the blade surface was documented in [9]. The blade is composed of a series of DU airfoils and the NACA64 profile.

We compute the case corresponding to wind speed of 11.4 m/s and rotor speed of 12.1 rpm. The air density and viscosity are 1.2 kg/m^3 and 2.0×10^{-5} kg/(m·s), respectively. The rotor has a radius of 63 m and is assumed to be rigid. We compute the aerodynamics of the wind turbine rotor using the ALE–VMS approach on a rotating mesh and compare the relative performance of the weak and strong boundary conditions for this significantly larger diameter wind turbine rotor design.

In the previous studies of this problem [9, 10, 18–20], both NURBS-based isogeometric and standard finite element discretizations with strongly enforced boundary conditions were employed. Also, a 120° slice of the computational domain with rotationally periodic boundary conditions [9,66,67] was used. Here, we consider a full domain of this three-bladed rotor without rotationally periodic boundary conditions. This choice was motivated by the fact that we are moving toward simulating the full wind turbine assembly, including the tower, for which rotationally periodic boundary conditions are no longer applicable.

The aerodynamics volume mesh is comprised of 6,309,349 linear tetrahedral elements and 1,193,404 nodes. Figure 9 shows a 2D blade cross-section at $0.75R$ to illustrate the coarse boundary layer mesh used in our computations. Near the blade surface, the size of the first element in the wall-normal direction is about 0.075 m. The Reynolds number based on the chord length and relative speed at $0.75R$ is $O(10^7)$, and the corresponding y^+ is $O(10^4)$.

The time history of the aerodynamic torque is plotted in Figure 10 for both weak and strong boundary condition simulations. The results are compared to the NURBS-based simulation from [19] and the NREL prediction from [2] obtained using FAST [1]. The weak boundary condition result is nearly identical to the NURBS-based simulation except for low-amplitude, high-frequency fluctuations present in the NURBS-based simulation, which better captures the fine-scale turbulence due to higher-order functions and better boundary-layer resolution employed. The strong boundary condition result in this study is, however, completely inaccurate. Nevertheless, as evident in [9,10,18–20], with sufficient boundary layer mesh refinement, strongly enforced boundary condition approach will capture the boundary layer and will also produce the correct result.

The comparison of the air speed and pressure contours at the blade cross-section corresponding to $0.75R$ for weakly and strongly enforced boundary condition simulations is shown in Figure 11. As in the case of the Phase VI rotor, the strong boundary condition simulation produces a thick boundary layer due to the lack of mesh refinement, which leads to unphysical flow separation, incorrect pressure distribution around the airfoil, and, as a result, inaccurate torque prediction.

Figure 12 shows the air speed contours (using the weak boundary condition formulation) in the rotor plane. As expected, the large scales of the air flow are very similar between the three blades. However, due to the fine-scale turbulence, the small-scale features show some differences and the flow is not fully periodic. Of course, the flow rotational periodicity will be further reduced in the presence of the tower.

4 Conclusions

We applied the ALE–VMS finite element formulation of aerodynamics to the simulation of wind turbines at full scale. The methodology was validated using the NREL Phase VI two-bladed rotor for which there exists an extensive set of experimental results. We found that the combination of ALE–VMS and weakly enforced boundary conditions are able to accurately predict the key quantities of engineering interest such as the aerodynamic torque and pressure distribution at the blade cross-sections even on meshes with coarse boundary layer refinement. We also applied the proposed methodology to the simulation of the NREL 5MW offshore baseline wind turbine rotor, with equally successful computational results. It should be noted that in all cases the *same* discrete formulation was employed.

It appears that independent of the flow conditions (turbulent, laminar, fully attached, partially attached, fully detached, etc.) and spatial scales employed (the NREL Phase VI rotor is 10 m in diameter, while the NREL 5MW offshore baseline wind turbine rotor is 126 m in diameter) the proposed ALE–VMS formulation with weakly enforced no-slip boundary conditions is able to predict the flow solution correctly. This is typically not the case for classical turbulence models, which need to be adjusted for every flow regime separately.

In the future work we plan to perform a more extensive testing of this configuration to cover the intermediate flow regimes, and possibly include rotor-tower interaction

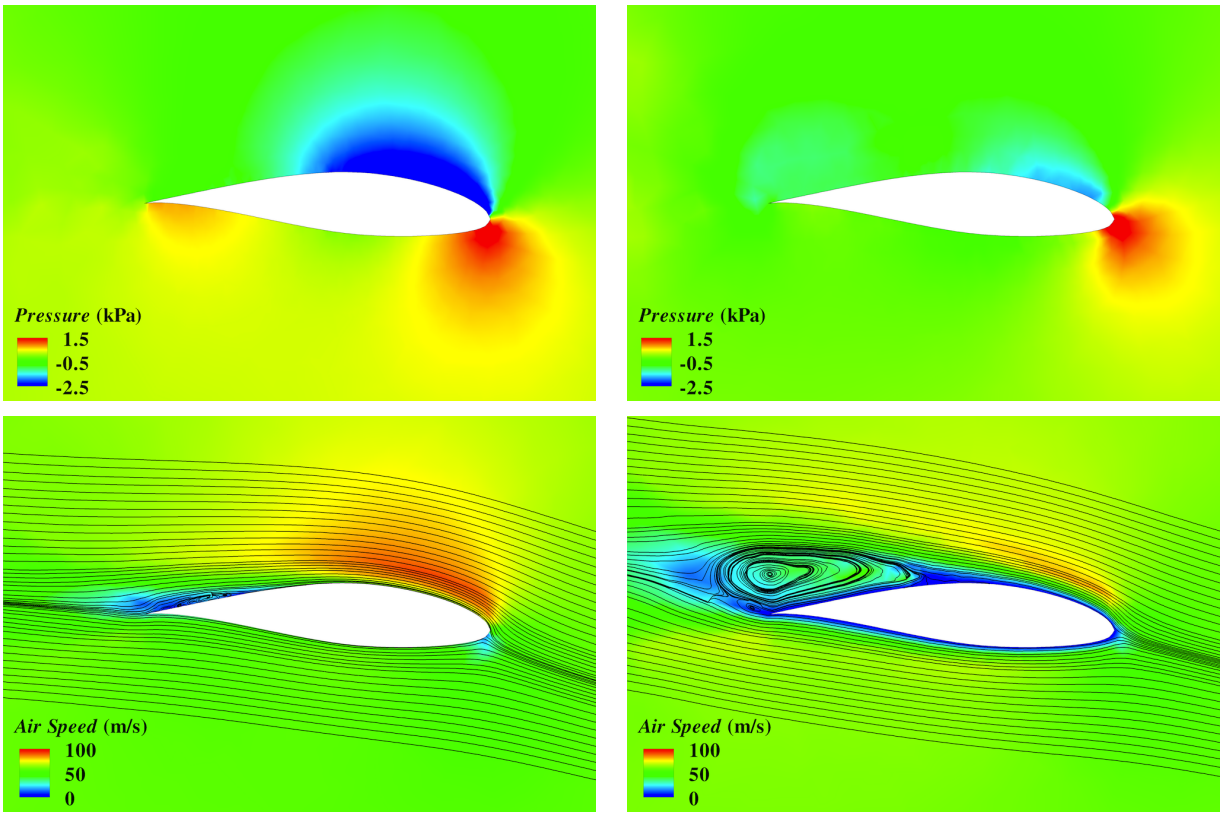

(a) Weakly enforced boundary condition (b) Strongly enforced boundary condition

Fig. 11 NREL 5MW offshore baseline wind turbine. Pressure and air speed contours and velocity streamlines at $0.75R$ for (a) weakly enforced boundary condition and (b) strongly enforced boundary condition simulations.

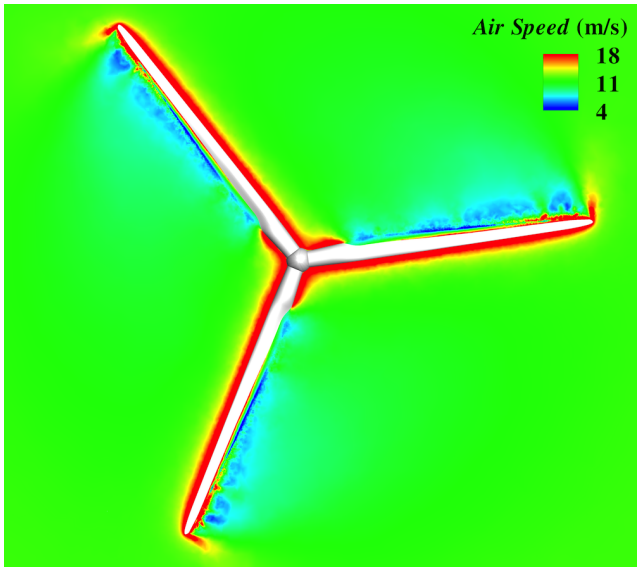

Fig. 12 NREL 5MW offshore baseline wind turbine. Air speed contours (using the weak boundary condition formulation) in the rotor plane. The large scales of the air flow are very similar between the three blades. However, the small-scale features show some differences and the flow is not fully periodic.

in these and other computations. Furthermore, a mesh refinement study may be valuable in order to better understand the behavior of the weak boundary condition formulation for different mesh resolution levels, as well as to better capture the details of turbulent flow.

Acknowledgement

We thank the Texas Advanced Computing Center (TACC) at the University of Texas at Austin for providing HPC resources that have contributed to the research results reported within this paper. M.-C. Hsu was supported by the Los Alamos–UC San Diego Educational Collaboration Fellowship. This support is gratefully acknowledged. Y. Bazilevs would like to acknowledge the support of the NSF CAREER Award.

References

1. J.M. Jonkman and M.L. Buhl Jr. FAST user's guide. Technical Report NREL/EL-500-38230, National Renewable Energy Laboratory, Golden, CO, 2005.
2. J. Jonkman, S. Butterfield, W. Musial, and G. Scott. Definition of a 5-MW reference wind turbine for offshore system development.

Technical Report NREL/TP-500-38060, National Renewable Energy Laboratory, Golden, CO, 2009.
3. N.N. Sørensen, J.A. Michelsen, and S. Schreck. Navier–Stokes predictions of the NREL Phase VI rotor in the NASA Ames 80 ft × 120 ft wind tunnel. *Wind Energy*, 5:151–169, 2002.
4. E.P.N. Duque, M.D. Burklund, and W. Johnson. Navier–Stokes and comprehensive analysis performance predictions of the NREL Phase VI experiment. *Journal of Solar Energy Engineering*, 125:457–467, 2003.
5. A. Le Pape and J. Lecanu. 3D Navier–Stokes computations of a stall-regulated wind turbine. *Wind Energy*, 7:309–324, 2004.
6. N. Sezer-Uzol and L.N. Long. 3-D time-accurate CFD simulations of wind turbine rotor flow fields. AIAA Paper 2006-0394, 2006.
7. F. Zahle and N.N. Sørensen. Overset grid flow simulation on a modern wind turbine. AIAA Paper 2008-6727, 2008.
8. F. Zahle, N.N. Sørensen, and J. Johansen. Wind turbine rotor-tower interaction using an incompressible overset grid method. *Wind Energy*, 12:594–619, 2009.
9. Y. Bazilevs, M.-C. Hsu, I. Akkerman, S. Wright, K. Takizawa, B. Henicke, T. Spielman, and T.E. Tezduyar. 3D simulation of wind turbine rotors at full scale. Part I: Geometry modeling and aerodynamics. *International Journal for Numerical Methods in Fluids*, 65:207–235, 2011.
10. K. Takizawa, B. Henicke, T.E. Tezduyar, M.-C. Hsu, and Y. Bazilevs. Stabilized space-time computation of wind-turbine rotor aerodynamics. *Computational Mechanics*, 48:333–344, 2011.
11. Y. Li, K.-J. Paik, T. Xing, and P.M. Carrica. Dynamic overset CFD simulations of wind turbine aerodynamics. *Renewable Energy*, 37:285–298, 2012.
12. E. Guttierez, S. Primi, F. Taucer, P. Caperan, D. Tirelli, J. Mieres, I. Calvo, J. Rodriguez, F. Vallano, G. Galiotis, and D. Mouzakis. A wind turbine tower design based on fibre-reinforced composites. Technical report, Joint Research Centre - Ispra, European Laboratory for Structural Assessment (ELSA), Institute For Protection and Security of the Citizen (IPSC), European Commission, 2003.
13. C. Kong, J. Bang, and Y. Sugiyama. Structural investigation of composite wind turbine blade considering various load cases and fatigue life. *Energy*, 30:2101–2114, 2005.
14. M.O.L. Hansen, J.N. Sørensen, S. Voutsinas, N. Sørensen, and H.Aa. Madsen. State of the art in wind turbine aerodynamics and aeroelasticity. *Progress in Aerospace Sciences*, 42:285–330, 2006.
15. F.M. Jensen, B.G. Falzon, J. Ankersen, and H. Stang. Structural testing and numerical simulation of a 34 m composite wind turbine blade. *Composite Structures*, 76:52–61, 2006.
16. J. Kiendl, Y. Bazilevs, M.-C. Hsu, R. Wüchner, and K.-U. Bletzinger. The bending strip method for isogeometric analysis of Kirchhoff–Love shell structures comprised of multiple patches. *Computer Methods in Applied Mechanics and Engineering*, 199:2403–2416, 2010.
17. Y. Bazilevs, M.-C. Hsu, J. Kiendl, and D.J. Benson. A computational procedure for pre-bending of wind turbine blades. *International Journal for Numerical Methods in Engineering*, 89:323–336, 2012.
18. Y. Bazilevs, M.-C. Hsu, J. Kiendl, R. Wüchner, and K.-U. Bletzinger. 3D simulation of wind turbine rotors at full scale. Part II: Fluid–structure interaction modeling with composite blades. *International Journal for Numerical Methods in Fluids*, 65:236–253, 2011.
19. M.-C. Hsu, I. Akkerman, and Y. Bazilevs. High-performance computing of wind turbine aerodynamics using isogeometric analysis. *Computers & Fluids*, 49:93–100, 2011.
20. K. Takizawa, B. Henicke, D. Montes, T.E. Tezduyar, M.-C. Hsu, and Y. Bazilevs. Numerical-performance studies for the stabilized space-time computation of wind-turbine rotor aerodynamics. *Computational Mechanics*, 48:647–657, 2011.
21. M.M. Hand, D.A. Simms, L.J. Fingersh, D.W. Jager, J.R. Cotrell, S. Schreck, and S.M. Larwood. Unsteady aerodynamics experiment phase VI: Wind tunnel test configurations and available data campaigns. Technical Report NREL/TP-500-29955, National Renewable Energy Laboratory, Golden, CO, 2001.
22. D. Simms, S. Schreck, M. Hand, and L.J. Fingersh. NREL unsteady aerodynamics experiment in the NASA–Ames wind tunnel: A comparison of predictions to measurements. Technical Report NREL/TP-500-29494, National Renewable Energy Laboratory, Golden, CO, 2001.
23. NREL 10 m Wind Turbine Testing in NASA Ames 80' × 120' Wind Tunnel. Available at: http://wind.nrel.gov/amestest/. Accessed October 6, 2011.
24. Y. Bazilevs, V.M. Calo, J.A. Cottrel, T.J.R. Hughes, A. Reali, and G. Scovazzi. Variational multiscale residual-based turbulence modeling for large eddy simulation of incompressible flows. *Computer Methods in Applied Mechanics and Engineering*, 197:173–201, 2007.
25. T.J.R. Hughes, J.A. Cottrell, and Y. Bazilevs. Isogeometric analysis: CAD, finite elements, NURBS, exact geometry and mesh refinement. *Computer Methods in Applied Mechanics and Engineering*, 194:4135–4195, 2005.
26. J.A. Cottrell, T.J.R. Hughes, and Y. Bazilevs. *Isogeometric Analysis: Toward Integration of CAD and FEA*. Wiley, Chichester, 2009.
27. Y. Bazilevs and T.J.R. Hughes. Weak imposition of Dirichlet boundary conditions in fluid mechanics. *Computers & Fluids*, 36:12–26, 2007.
28. Y. Bazilevs, C. Michler, V.M. Calo, and T.J.R. Hughes. Weak Dirichlet boundary conditions for wall-bounded turbulent flows. *Computer Methods in Applied Mechanics and Engineering*, 196:4853–4862, 2007.
29. Y. Bazilevs, C. Michler, V.M. Calo, and T.J.R. Hughes. Isogeometric variational multiscale modeling of wall-bounded turbulent flows with weakly enforced boundary conditions on unstretched meshes. *Computer Methods in Applied Mechanics and Engineering*, 199:780–790, 2010.
30. Y. Bazilevs and I. Akkerman. Large eddy simulation of turbulent Taylor–Couette flow using isogeometric analysis and the residual–based variational multiscale method. *Journal of Computational Physics*, 229:3402–3414, 2010.
31. J. Nitsche. Über ein variationsprinzip zur Lösung von Dirichlet-Problemen bei Verwendung von Teilräumen, die keinen Randbedingungen unterworfen sind. *Abh. Math. Univ. Hamburg*, 36:9–15, 1971.
32. D.N. Arnold, F. Brezzi, B. Cockburn, and L.D. Marini. Unified analysis of Discontinuous Galerkin methods for elliptic problems. *SIAM Journal of Numerical Analysis*, 39:1749–1779, 2002.
33. Y. Bazilevs, V.M. Calo, T.J.R. Hughes, and Y. Zhang. Isogeometric fluid–structure interaction: theory, algorithms, and computations. *Computational Mechanics*, 43:3–37, 2008.
34. C. Johnson. *Numerical solution of partial differential equations by the finite element method*. Cambridge University Press, Sweden, 1987.
35. S.C. Brenner and L.R. Scott. *The Mathematical Theory of Finite Element Methods, 2nd ed.* Springer, 2002.
36. A. Ern and J.-L. Guermond. *Theory and Practice of Finite Elements*. Springer, 2004.
37. A.N. Brooks and T.J.R. Hughes. Streamline upwind/Petrov–Galerkin formulations for convection dominated flows with particular emphasis on the incompressible Navier–Stokes equations. *Computer Methods in Applied Mechanics and Engineering*, 32:199–259, 1982.
38. T.J.R. Hughes and T.E. Tezduyar. Finite element methods for first-order hyperbolic systems with particular emphasis on the compressible Euler equations. *Computer Methods in Applied Mechanics and Engineering*, 45:217–284, 1984.

39. T.E. Tezduyar and Y.J. Park. Discontinuity capturing finite element formulations for nonlinear convection-diffusion-reaction equations. *Computer Methods in Applied Mechanics and Engineering*, 59:307–325, 1986.
40. T.J.R. Hughes, L.P. Franca, and M. Balestra. A new finite element formulation for computational fluid dynamics: V. Circumventing the Babuška–Brezzi condition: A stable Petrov–Galerkin formulation of the Stokes problem accommodating equal-order interpolations. *Computer Methods in Applied Mechanics and Engineering*, 59:85–99, 1986.
41. T.E. Tezduyar and Y. Osawa. Finite element stabilization parameters computed from element matrices and vectors. *Computer Methods in Applied Mechanics and Engineering*, 190:411–430, 2000.
42. T.E. Tezduyar. Computation of moving boundaries and interfaces and stabilization parameters. *International Journal for Numerical Methods in Fluids*, 43:555–575, 2003.
43. T.J.R. Hughes, G. Scovazzi, and L.P. Franca. Multiscale and stabilized methods. In E. Stein, R. de Borst, and T.J.R. Hughes, editors, *Encyclopedia of Computational Mechanics, Vol. 3, Fluids*, chapter 2. Wiley, 2004.
44. K. Takizawa and T.E. Tezduyar. Multiscale space–time fluid–structure interaction techniques. Computational Mechanics, 2011.
45. T.J.R. Hughes. Multiscale phenomena: Green's functions, the Dirichlet-to-Neumann formulation, subgrid scale models, bubbles, and the origins of stabilized methods. *Computer Methods in Applied Mechanics and Engineering*, 127:387–401, 1995.
46. T.J.R. Hughes, G.R. Feijóo, L. Mazzei, and J.-B. Quincy. The variational multiscale method–A paradigm for computational mechanics. *Computer Methods in Applied Mechanics and Engineering*, 166:3–24, 1998.
47. T.J.R. Hughes and G. Sangalli. Variational multiscale analysis: the fine-scale Green's function, projection, optimization, localization, and stabilized methods. *SIAM Journal of Numerical Analysis*, 45:539–557, 2007.
48. D.D. Chao and C.P. van Dam. CFD analysis of rotating two-bladed flatback wind turbine rotor. Sandia Report SAND2008-1688, Sandia National Laboratories, Albuquerque, NM, 2008.
49. B.E Launder and D.B. Spalding. The numerical computation of turbulent flows. *Computer Methods in Applied Mechanics and Engineering*, 3:269–289, 1974.
50. D.C. Wilcox. *Turbulence Modeling for CFD*. DCW Industries, La Canada, CA, 1998.
51. J.M. Jonkman. Modeling of the UAE wind turbine for refinement of FAST_AD. Technical Report NREL/TP-500-34755, National Renewable Energy Laboratory, Golden, CO, 2003.
52. J. Johansen, N.N. Sørensen, J.A. Michelsen, and S. Schreck. Detached-eddy simulation of flow around the NREL Phase VI blade. *Wind Energy*, 5:185–197, 2002.
53. D.J. Laino, A.C. Hansen, and J.E. Minnema. Validation of the AeroDyn subroutines using NREL Unsteady Aerodynamics Experiment data. *Wind Energy*, 5:227–244, 2002.
54. C. Tongchitpakdee, S. Benjanirat, and L.N. Sankar. Numerical simulation of the aerodynamics of horizontal axis wind turbines under yawed flow conditions. *Journal of Solar Energy Engineering*, 127:464–474, 2005.
55. S. Schmitz and J.-J. Chattot. Characterization of three-dimensional effects for the rotating and parked NREL Phase VI wind turbine. *Journal of Solar Energy Engineering*, 128:445–454, 2006.
56. M.A. Potsdam and D.J. Mavriplis. Unstructured mesh CFD aerodynamic analysis of the NREL Phase VI rotor. AIAA Paper 2009-1221, 2009.
57. S. Gómez-Iradi, R. Steijl, and G.N. Barakos. Development and validation of a CFD technique for the aerodynamic analysis of HAWT. *Journal of Solar Energy Engineering*, 131:031009–1–13, 2009.
58. J.-C. Huang, H. Lin, T.-J. Hsieh, and T.-Y. Hsieh. Parallel preconditioned WENO scheme for three-dimensional flow simulation of NREL Phase VI rotor. *Computers & Fluids*, 45:276–282, 2011.
59. Texas Advanced Computing Center (TACC). Available at: http://www.tacc.utexas.edu. Accessed October 6, 2011.
60. Longhorn User Guide. Available at: http://www.tacc.utexas.edu/user-services/user-guides/longhorn-user-guide. Accessed October 6, 2011.
61. G. Karypis and V. Kumar. A fast and high quality multilevel scheme for partitioning irregular graphs. *SIAM Journal on Scientific Computing*, 20:359–392, 1999.
62. J. Chung and G. M. Hulbert. A time integration algorithm for structural dynamics with improved numerical dissipation: The generalized-α method. *Journal of Applied Mechanics*, 60:371–75, 1993.
63. K.E. Jansen, C.H. Whiting, and G.M. Hulbert. A generalized-α method for integrating the filtered Navier-Stokes equations with a stabilized finite element method. *Computer Methods in Applied Mechanics and Engineering*, 190:305–319, 2000.
64. Y. Saad and M.H. Schultz. GMRES: A generalized minimal residual algorithm for solving nonsymmetric linear systems. *SIAM Journal of Scientific and Statistical Computing*, 7:856–869, 1986.
65. F. Shakib, T.J.R. Hughes, and Z. Johan. A multi-element group preconditioned GMRES algorithm for nonsymmetric systems arising in finite element analysis. *Computer Methods in Applied Mechanics and Engineering*, 75:415–456, 1989.
66. K. Takizawa, C. Moorman, S. Wright, T. Spielman, and T.E. Tezduyar. Fluid–structure interaction modeling and performance analysis of the Orion spacecraft parachutes. *International Journal for Numerical Methods in Fluids*, 65:271–285, 2010.
67. K. Takizawa, S. Wright, C. Moorman, and T.E. Tezduyar. Fluid–structure interaction modeling of parachute clusters. *International Journal for Numerical Methods in Fluids*, 65:286–307, 2010.